Column-integrated aerosol optical properties in Sodankylä (Finland) during the Solar Induced Fluorescence Experiment (SIFLEX-2002)

José L. Gómez-Amo,[1] José A. Martínez-Lozano,[1] María P. Utrillas,[1] Roberto Pedrós,[1] and Victor Estellés[1]

Received 6 April 2005; revised 18 October 2005; accepted 17 November 2005; published 7 March 2006.

[1] A study has been made of the column aerosols using solar irradiance extinction measurements at ground level in a boreal region (Sodankylä, Finland) during spring 2002. The aerosol properties have been related to air mass origin. In general, the aerosol levels were observed to be very low, independent of the air mass origin, with an aerosol optical depth (AOD) value at 500 nm of less than 0.09 ± 0.03. Two characteristic patterns were observed depending on whether the air masses originated in the north and west or from the south and east. In the first case (north and west origins) the aerosol load was very small, with very low optical depths in the range 0.03 ± 0.02 to 0.09 ± 0.03 for 500 nm wavelengths. The size distribution usually showed two modes, with a strong contribution from the large-particle mode, probably a consequence of the presence of maritime-type particles originating in the ocean. When the air masses originated from a south or east direction, the behavior was the opposite to that noted before. In these cases the AOD was rather larger, above all for air masses originating in central Europe and Russia with an average value at 500 nm of 0.14 ± 0.02.

Citation: Gómez-Amo, J. L., J. A. Martínez-Lozano, M. P. Utrillas, R. Pedrós, and V. Estellés (2006), Column-integrated aerosol optical properties in Sodankylä (Finland) during the Solar Induced Fluorescence Experiment (SIFLEX-2002), *J. Geophys. Res.*, *111*, D05202, doi:10.1029/2005JD006051.

1. Introduction

[2] For global change studies, understanding the role of forests as sinks and sources of carbon dioxide, the most challenging greenhouse gas, is of utmost importance. The carbon balance of a forest is the difference between the gross primary production (GPP) and the total respiration. A great effort has been made to quantify these components because the information is needed for the estimation and verification of carbon sinks according to the Kyoto Protocol.

[3] Remote sensing is the only tool for achieving a homogeneous analysis on a large scale. Presently there are estimations of GPP from remote sensing observations using simple methods based on the measurements of fractional absorbed photosynthetically active radiation (fAPAR) and incident solar radiation covering the photosynthetic photon flux density (PPFD).

[4] The photosynthetic yield has been measured by chlorophyll fluorescence instruments, which give information on the down regulation of the photochemical apparatus, for example, due to dormancy, water stress or excess solar radiation. Fluorescence has been measured traditionally, using excitation light pulses by photodiodes, flash light or lasers. Solar-induced, passive fluorescence could offer a remote sensing method to obtain direct information on the activity of photochemistry, which is a key factor to improve the estimates of the GPP, the water stress or the vitality of the plants.

[5] Validation of the fluorescence signals for different plant types and environments on canopy level is urgently needed. For this purpose, the European Space Agency organized the first field campaign, Solar Induced Fluorescence Experiment (SIFLEX-2002) [*European Space Agency*, 2002], for observing solar-induced fluorescence in a boreal forest during the spring recovery of Scots pine. The campaign is part of the FLEX studies funded by ESA, originally proposed as a Fluorescence Mission to explore the feasibility of the detection and scientific use of the remote sensed fluorescence of terrestrial vegetation by *Stoll et al.* [1999a, 1999b].

[6] The main goal of this SIFLEX campaign was to understand whether solar-induced fluorescence measurements may someday be used to monitor and map the photochemical activity of boreal forests from space. More specifically, the objectives were as follows: (1) to measure and quantify the solar-induced fluorescence flux in the A and B oxygen absorption bands during spring thaw in a boreal forest; (2) to measure the global and direct energy incident over the boreal forest; (3) to collect complementary atmospheric measurements for fluorescence interpretation and radiative modeling purposes; and (4) to collect a CO_2 flux data set for the study of linkage between photosynthetic activity indicators and CO_2.

[1] Solar Radiation Group, University of Valencia, Burjassot, Spain.

0148-0227/06/2005JD006051$09.00

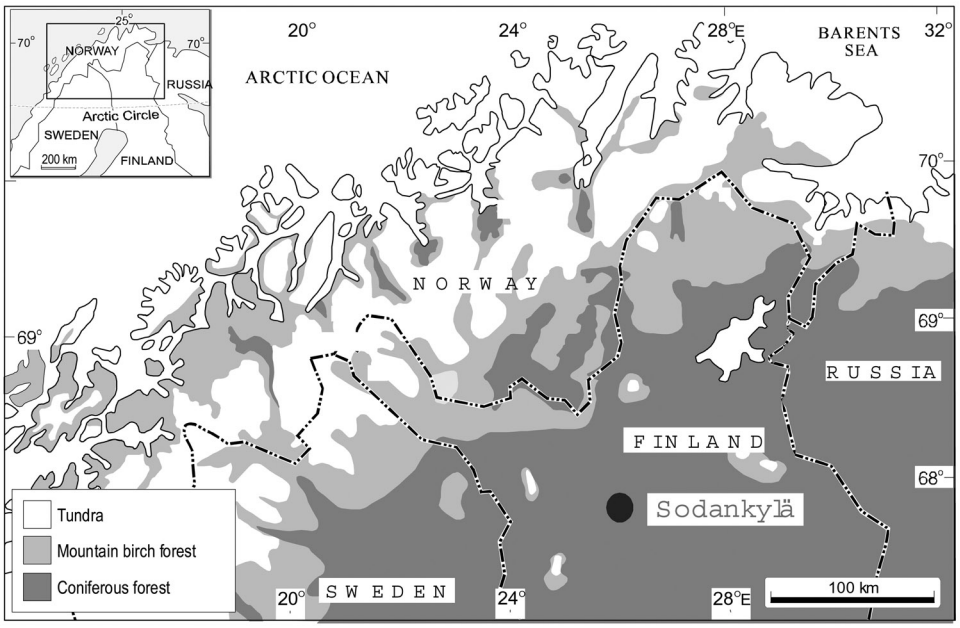

Figure 1. Sodankylä, measurement site [*Davidson et al.*, 2002].

[7] This work looks at one of the aspects of point 3, the characterization of the atmospheric aerosols during the campaign, giving special emphasis to (1) their spectral optical depth; (2) the values taken by the Angstrom wavelength exponent (α); and (3) their size distribution and its relation to the origin of the air masses of the measurement site.

[8] Season and location are only partial predictors of aerosol optical properties, while aerosol size, for instance, can vary significantly from day to day at a single location [*Holben et al.*, 1996; *Remer and Kaufman*, 1998]. Such day-to-day variations stem from meteorological variability rather than direct changes in the strength of aerosol sources. Aerosol optical properties are particularly dependent on the air mass residence times and the duration of stagnant conditions [*Remer et al.*, 1999]. More information (and more detailed) is needed on the atmospheric aerosols' optical and radiative properties and their distribution in space and time [*Schwartz and Andreae*, 1996; *Penner et al.*, 2001].

[9] One of the most reliable means of determining the optical and physical properties of the total aerosol column is the combination of two methods: airborne in situ measurements and ground-based remote sensing [*Remer et al.*, 1997]. In this paper we present the results corresponding to the column integrated aerosol optical properties over the Sodankylä area during all the days of the SIFLEX campaign. We have started from the determination of the aerosol optical depth (hereafter AOD) from solar irradiance extinction measurements at ground level. The AOD is the single most comprehensive variable to remotely assess the aerosol burden in the atmosphere from ground based instruments, which are the simplest, most accurate and easy to maintain monitoring system [*Holben et al.*, 2001].

2. Field Campaign

[10] The European Space Agency made contracts with three institutes for conducting the SIFLEX-2002 campaign. The participating institutes were (1) Laboratoire pour l'Utilisation du Rayonnement Electromagnetiqué (LURE), Paris, France; (2) University of Valencia, Valencia, Spain; and (3) Finnish Meteorological Institute (FMI), Helsinki, Finland.

[11] LURE had the most demanding task of developing methods and observations of chlorophyll fluorescence using passive and active methods. The central tasks of the University of Valencia team were studies of the atmospheric components characteristics and spectral observations of sky radiation and radiation reflected from the forests, including the shortwave and infrared regions of the spectra. FMI provided the observations of CO_2 fluxes between the forest and the atmosphere and also the infrastructure.

[12] The measurements corresponding to the SIFLEX-2002 campaign were carried out at the Arctic Research Centre of the Finnish Meteorological Institute in the North Boreal zone, 100 km north of the Arctic Circle (67°21′43″ latitude, 26°38′16″ longitude, 179 m above sea level) (see Figure 1). The Research Centre is located close to the river Kitinen in a Scots pine forest, typical of the ecosystems in the area. Pine is the most common tree species in Lapland, with forests dominated by Scots pine covering 75% of the forest land area. The nearest town to the Research Centre, Sodankylä, is 7 km away, while the nearest larger town with an average population density, Rovaniemi, is 150 km away.

[13] At the observatory, routine meteorological observations include for example synoptic weather reports, PTU soundings, a weekly ozone sounding and continuously recorded UV spectral radiation and broadband radiation components and meteorological parameters. Close to the Research Centre, carbon dioxide exchange between the atmosphere and the Scots pine forest are measured using the micrometeorological eddy covariance method [*Aurela et al.*, 2002; *Laurila et al.*, 2001] with a half-hourly resolution as part of a CARBOEUROPE study (http://www.carboeurope.org). Downward and reflected solar radiation and PPFD, net radiation, and gradients of the CO_2 concentration, temperature, humidity and wind speed are measured at a

Table 1. Monthly Averages of Temperature, Precipitation, Cloudiness, and Snow Depth (1961–1990) and Global Radiation (1981–1990) at the Arctic Research Centre of the Finnish Meteorological Institute (Sodankylä, Finland)

	Air Temperature, °C	Precipitation, mm	Cloudiness, %	Snow Depth on Fifteenth, cm	Global Radiation, MJ m^{-2}
Jan.	−15.1	30.7	74	51	6
Feb.	−15.6	25.5	74	67	50
March	−8.5	25.2	70	72	176
April	−2.1	23.6	68	69	389
May	5.0	34.5	70	15	490
June	11.6	55.9	71		542
July	14.1	64.7	70		497
Aug.	11.2	62.8	75		342
Sept.	5.9	55.3	78		175
Oct.	−0.3	50.9	80	3	64
Nov.	−7.4	39.4	79	15	12
Dec.	−13.1	30.8	74	34	1

48-m-high micrometeorological mast. The fluxes of CO_2, latent and sensible heat and momentum are measured at a height of 23 m.

[14] In the Köppen climate classification [*Strahler and Strahler*, 1992], northern Finland belongs to an area of snow and forest climate characterized by moist, cold winters. Yearly averages (1961–1990) of temperature and precipitation are −1.0°C and 500 mm, respectively. The monthly averages of air and soil temperature, precipitation, cloudiness and snow depth on the fifteenth day of the month and the monthly accumulated global radiation show very seasonal changes typical of the boreal area (Table 1).

[15] For the SIFLEX campaign a period from the end of April to the beginning of June was chosen. Weather at the end of April is usually characterized by freezing temperatures, at least during the night, high snow depth and soil frost. The principal instrument used for characterizing the column aerosols was a LI-COR 1800 spectroradiometer with a simple monochromator and a halographic grating with 600 grooves/mm, which operates in the 300–1100 nm spectral range. The optical receiver is a Teflon dome with a 2π steradian field of view (FOV). The slit function of the instrument is determined in the laboratory by shining fixed wavelength radiation on the spectroradiometer and measuring a series of very close wavelengths. The bandwidth (FWHM) of the instrument is 6 nm and the band step is 1 nm. The detector is a silicon photodiode operating in photovoltaic mode. For the measurement of direct irradiance a collimator was used with a 4.6° FOV fitted with an alignment system that coupled directly to the Teflon diffuser. The spectroradiometer was manually oriented, mounted on a tripod with three ball-and-socket joints that allowed rotation around the three axes. The uncertainty associated with this instrument in the working range (340–1020 nm) is about 5% [*Martínez-Lozano et al.*, 2003], a value that includes uncertainties due both to the calibration and the measurement process. The LI-COR is regularly calibrated every 6 months using an absolute calibration lamp (LI-COR optical radiation calibration). In this case it was calibrated on the days before the campaign and again following the campaign. The spectroradiometer was installed on an 18-m-high tower with most of the other solar radiation measuring equipment with a totally open horizon.

[16] We also used a Microtops II, a portable photometer which operates with five channels and is capable of directly providing the total ozone content, the water vapor content and the aerosol optical depth at 1020 nm in the whole atmospheric column. Three of these channels are for measuring ozone (305.5, 312.5, 320 nm), the 940 nm channel is for precipitable water vapor and the 1020 nm channel for aerosol optical depth measurement (although in this work these measurements have not been considered). Each of these channels has a collimator with a field of view of 2.5° and deflectors to remove internal reflections. Furthermore, it incorporates a narrow band interferential filter and a photodiode tailored to each band. The inaccuracy due to nonlinearity is kept below 0.002% and the combined precision is between 1 and 2% [*Morys et al.*, 2001].

[17] Solar direct irradiance measurements were acquired on 14 whole days (clear skies) with the LI-COR 1800. The measurements were made every 15 min from 0700 to 1300 UTC and then every hour till 1800 UTC. The Microtops II measurements were made at the same times.

3. Air Mass Analysis

[18] Information on the origin and type of air mass reaching the study zone is necessary in order to better understand and interpret the characteristics of the aerosols present in the atmosphere during the measurement campaign. To determine the air mass origin, and to account for the possible aerosol transport and their precedence, the back trajectories were examined for each day of the campaign for which spectral irradiance measures were available. These back trajectories were obtained using the Hybrid Single Particle Lagrangian Integrated Trajectory (HYSPLIT) model developed by the National Oceanic and Atmospheric Administration (R. R. Draxler and G. D. Rolph, HYSPLIT (Hybrid Single-Particle Lagrangian Integrated Trajectory), 2003, available from NOAA ARL READY Web site at http://www.arl.noaa.gov/ready/hysplit4.html). The period considered for the back trajectories was five days.

[19] Since the aerosol properties observed from the solar irradiance extinction measurements refer to the whole atmospheric column, three altitudes were considered for estimating the origins of the air masses. The first was within

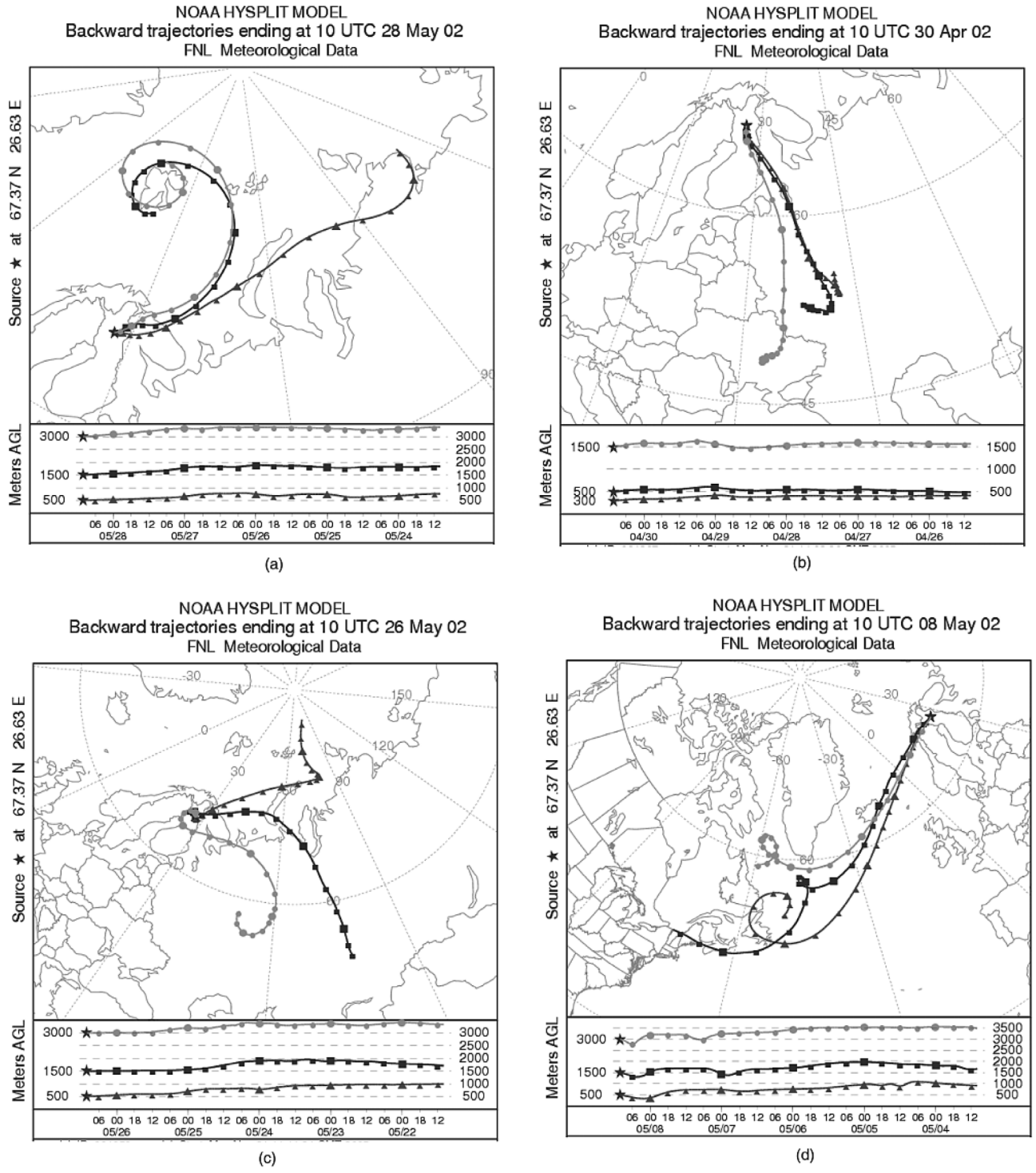

Figure 2. Air mass back trajectories: (a) coming from the north, 28 May 2002; (b) coming from the south, 30 April 2002; (c) coming from the east, 26 May 2002; and (d) coming from the west, 8 May 2002.

the mixture layer (500 m), the second near the top of the same layer (1500 m) and the last in the lowest layer of the free troposphere (3000 m). Both the isentropic and the isobaric trajectories were examined in order to check consistency before accepting the calculated trajectories. Furthermore the back trajectories for three different times of day (0700, 1000 and 1300 UTC) were calculated to check diurnal stability.

[20] According to *Valkama and Rossi* [1992] and *Rummukainen et al.* [1996], the region is subject to the influence of various air masses that arrive from different directions. *Ricard et al.* [2002a, 2002b] have classified the origins of

Table 2. Air Mass Origin, Average Daily Values of Relative Humidity, and a Hypothesis of the Aerosol Type

Day	Air Mass Origin	From	RH, %	Possible Aerosol Type
28 April 2002	south	Russia	57	continental
30 April 2002	south	Russia and central Europe	85	continental
4 May 2002	west	Atlantic Ocean, North Sea, and Scandinavia	63	marine and continental
8 May 2002	west	Atlantic Ocean and Scandinavia	54	marine and continental
15 May 2002	south	Europe and Scandinavia	72	marine and continental
23 May 2002	north	Arctic Ocean	47	Arctic (marine)
26 May 2002	east	Arctic Ocean and Russia	62	marine and continental
27 May 2002	east	Arctic Ocean and Russia	52	marine and continental
28 May 2002	north	Arctic Ocean and Kola Peninsula	37	Arctic and sulfate
29 May 2002	north	Arctic Ocean, Kola Peninsula, and local	34	Arctic and sulfate
30 May 2002	north	Arctic Ocean, Kola Peninsula, and local	33	Arctic and sulfate
31 May 2002	north	Arctic Ocean, Kola Peninsula, and local	31	Arctic and sulfate
1 June 2002	south	Scandinavia and Russia	45	continental
7 June 2002	south	Russia and Scandinavia	68	continental

these masses according to the direction they come from and the components that they carry, proposing the following:

[21] 1. The winds from the north bring clean air, of maritime origin, proceeding from the Arctic Ocean and the Barents Sea. Sometimes it is possible to find aerosols of anthropogenic origin because the air masses coming from the north use to cross over the Kola Peninsula, which is an important industrial area. Figure 2a shows the back trajectories for 28 May with this origin.

[22] 2. The winds coming from the south can transport air masses whose origin is in central Europe or Russia, generally associated with anthropogenic chemical species. In the summer season and under anticyclonic conditions these winds are dominated by local biogenic emissions. Figure 2b shows back trajectories of this type corresponding to 30 April. In this case the isentropic curves obtained follow straight lines, indicating high atmospheric stability.

[23] 3. The winds from the east bring marine origin air masses from the White Sea, although generally these pass over the Kola Peninsula where there is an important Russian industrial region that is responsible for approximately 20% of the emission of SO_2 north of the Arctic Circle [*Tuovinen et al.*, 1993]. As for the previous case, under anticyclonic conditions the local biogenic emissions are predominant in summer. Figure 2c shows back trajectories for these conditions corresponding to 26 May.

[24] 4. The winds from the west usually transport marine origin air masses coming from the Atlantic Ocean that generally pass over the Scandinavian Peninsula. Figure 2d shows back trajectories corresponding to 8 May.

[25] The classification mentioned above may seem to be too broad, but taking into account that there are only 14 days of measurements is difficult to classify the air masses in more than four regions.

[26] Furthermore, according to the classification made by *Ruellan* [2000], taking into account their origin and based on trace components (sodium for maritime origin and black carbon for continental origin), air masses can be classified into three types: (1) purely maritime, (2) purely continental, and (3) a mix of both. Generally, the mix of both continental and maritime predominate, a fact that is even more evident during the spring, the period during which our measurement campaign took place. However, during the campaign no chemistry measurements were available to clarify the influence of various source regions at the same time.

[27] During the campaign, in general no significant differences were observed in the origins of the air masses when considering the three different times of day. As a result, Table 2 only shows the characteristics of the back trajectories for 1000 UTC, as obtained for each day of the campaign for which measurements were available, these back trajectories being representative of the whole day. In the third column of the table appear the most relevant zones passed over by the air masses. The table also shows the relative humidity (RH) and proposes a possible hypothesis for the type of transported aerosols.

[28] Following the classification of *Ruellan* [2000], of the 14 days of the campaign with valid observations the air masses of four could be classed as purely continental in origin, while only one day could be classed as purely maritime. All the other nine days were classified as a mixture of the two.

[29] In general, when the air masses came from the south the aerosols that reached the study area were of continental type, since in only one case was a mixture of continental and maritime aerosols observed. On the other hand, following the classification of *Ricard et al.* [2002a, 2002b], if the aerosols arrived from the north they should have contained maritime-type aerosols while our observations indicate a mixed origin between maritime and continental. Later we analyze the different aerosol properties obtained from the experimental measurements and relate these to the air mass origins.

[30] As well as these characteristic trajectories of the air masses, in the Arctic it is usual to find a phenomenon known as ''Arctic haze.'' This is an increase in the pollution by anthropogenic aerosols normally coming from central Europe and Russia [*Shaw*, 1982; *Khattatov et al.*, 1997; *Heintzenberg*, 1980]. *Herber et al.* [2002], on the basis of a study of the properties of Arctic aerosols in Spitsbergen (78.95°N, 11.95°E), characterize this ''Arctic haze'' phenomenon by the presence of aerosols coming from continental Europe with an AOD of 0.094 at 532 nm. The phenomenon is most pronounced at the end of winter and the beginning of spring, from the end of March and through April. In our case, and on the basis of the AOD values at 500 nm, it could be considered that ''Arctic haze'' was

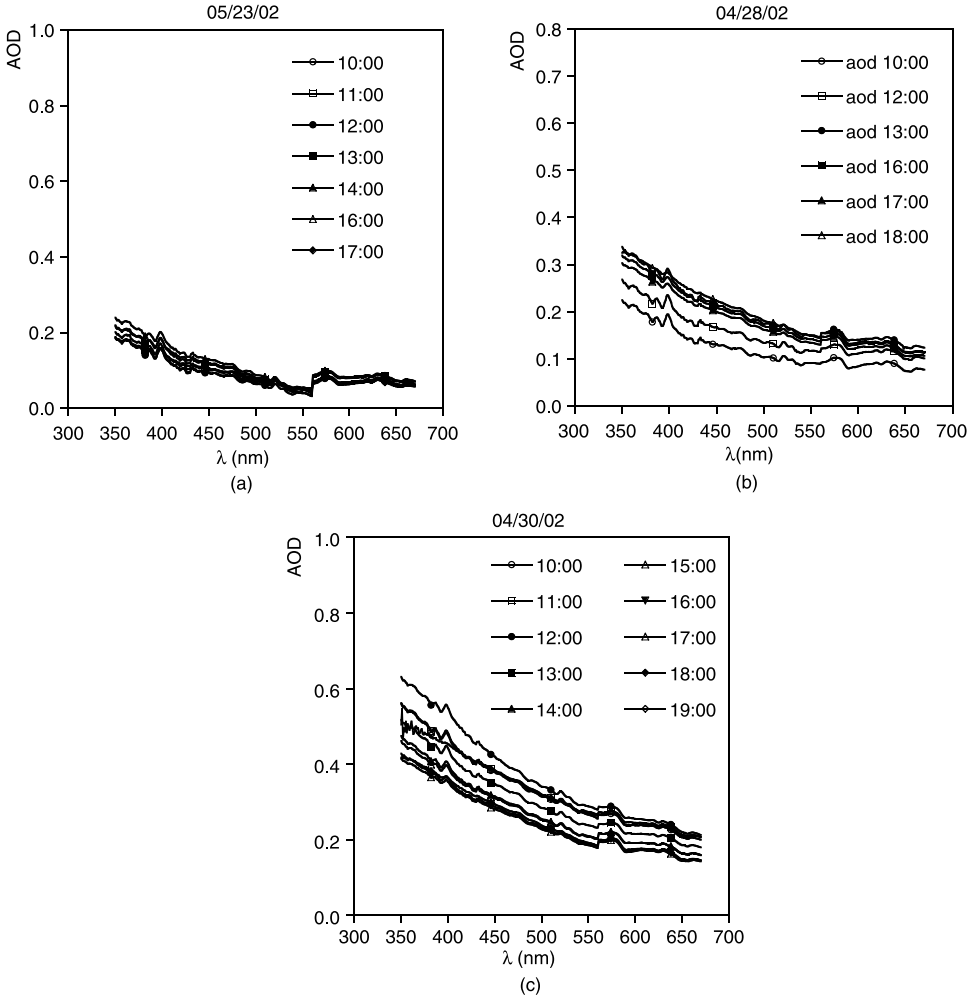

Figure 3. Spectral AOD for different times of day, (a) 23 May 2002, (b) 28 April 2002, and (c) 30 April 2002.

present on 28 and 30 April. We will consider later the sounding data available at Sodankylä Observatory (twice per day) in order to determine the existence of a residual layer on these two days.

4. Methodology

4.1. Aerosol Optical Depth

[31] The aerosol optical depth (AOD) can be obtained as the immediate result of atmospheric solar radiation extinction measurements by employing the Bouguer-Lambert-Beer law and eliminating the contribution of the gaseous components in the relevant spectral range. The spectral interval available for the instrument ranges from 300 nm to 1100 nm. However, only the 340–1020 nm interval, where the instrument error is least, was used. In this interval the only components that show appreciable absorption are ozone (Chappuis band), NO_2 and water vapor. Thus the total atmospheric optical depth can be expressed as

$$k_T(\lambda) = k_R(\lambda) + k_{O_3}(\lambda) + k_{NO_2}(\lambda) + k_w(\lambda) + AOD(\lambda) \quad (1)$$

where $k_R(\lambda)$ is the optical depth due to molecular scattering (Rayleigh scattering), and $k_{O3}(\lambda)$, $k_{NO2}(\lambda)$ and $k_W(\lambda)$ are

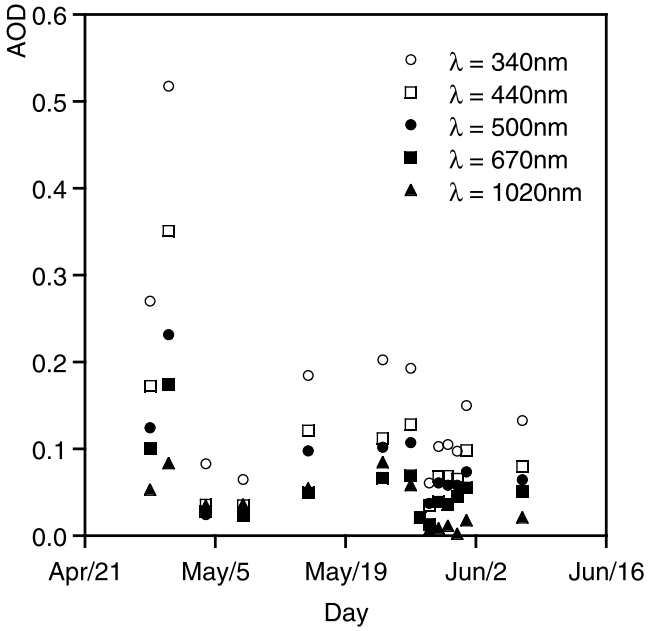

Figure 4. Evolution over the whole campaign of the AOD for wavelengths 340, 440, 500, 670, and 1020 nm.

Table 3. AOD at 500 nm for Each Day of the Measurement Campaign

Day	AOD (500 nm)
28 April 2002	0.14 ± 0.02
30 April 2002	0.28 ± 0.02
4 May 2002	0.03 ± 0.02
8 May 2002	0.03 ± 0.02
15 May 2002	0.10 ± 0.03
23 May 2002	0.09 ± 0.03
26 May 2002	0.11 ± 0.02
27 May 2002	0.08 ± 0.03
28 May 2002	0.02 ± 0.03
29 May 2002	0.06 ± 0.03
30 May 2002	0.06 ± 0.03
31 May 2002	0.05 ± 0.03
1 June 2002	0.08 ± 0.03
7 June 2002	0.07 ± 0.03

the optical depths due to absorption by ozone, NO_2 and water vapor, respectively.

[32] To determine the total atmospheric optical depth, the extraterrestrial spectrum proposed by the SMART2 [*Gueymard*, 2001] model was used after smoothing for the LI-COR 1800 bandwidth. The optical mass was obtained from the empirical relation proposed by *Kasten and Young* [1989]. The contribution due to Rayleigh scattering was calculated using the approximation of *Bodhaine et al.* [1999]. The coefficients used for the ozone absorption were those proposed by *Anderson and Mauersberger* [1992], while the expressions and coefficients used to calculate the water vapor and NO_2 absorption were taken from the SMART2 model [*Gueymard*, 2001], although the amounts of this latter gas were almost negligible because of the rural nature of the measurement site. Finally, water vapor and ozone measurements were also made with the Microtops II.

[33] Error propagation methods were applied to obtain the AOD error. *Utrillas* [1995] developed a simplified method to estimate the error associated with the AOD values retrieved from spectral irradiance measurements. This method is similar to that developed by *Russell et al.* [1993] and *Schmid et al.* [1999]. In our case the error in the AOD is mainly conditioned by the error in the measurement of the direct spectral irradiance and the value of the optical air mass at the instant of the measurement. The authors have previously used this method with experimen-

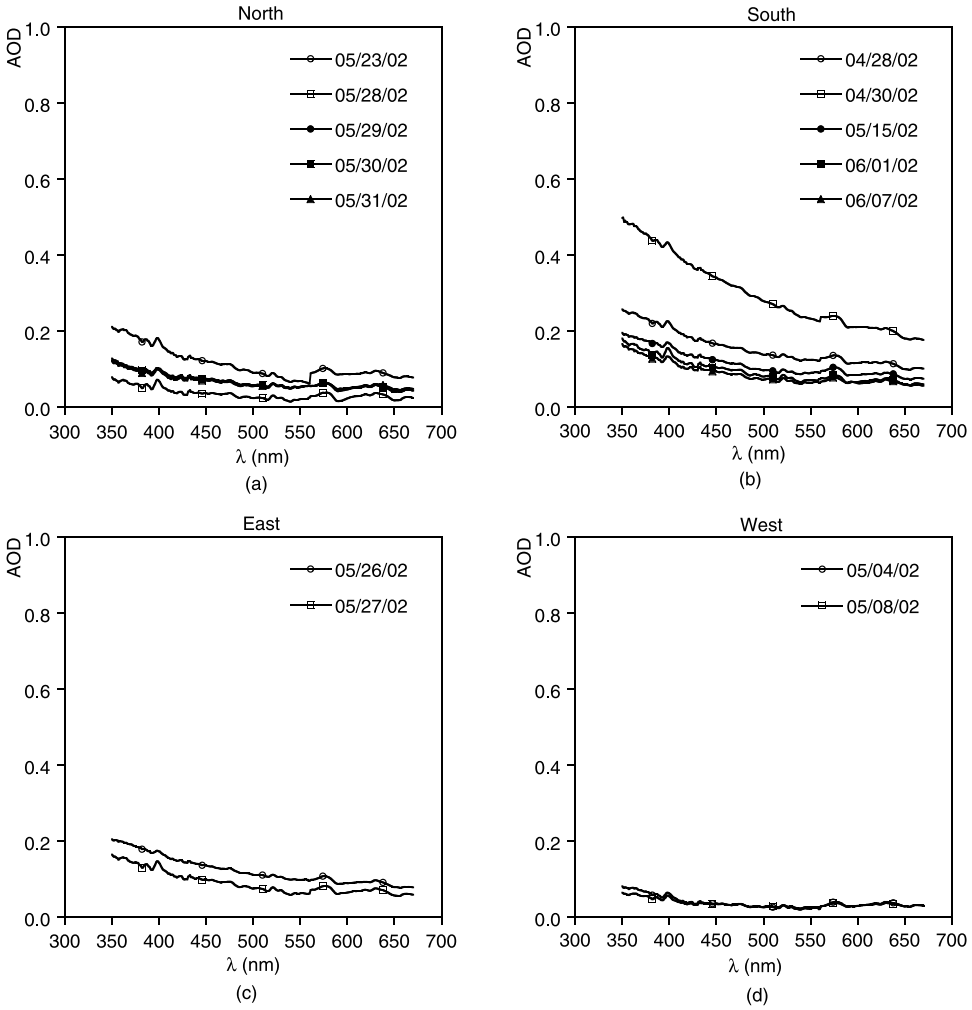

Figure 5. (a–d) Average spectral AOD classified according to air mass origin.

Table 4. AOD Values at 500 nm According to Air Mass Origin

Air Mass Origin	AOD Mean	AOD Min[a]	AOD Max[a]
North	0.06 ± 0.03	0.02 ± 0.03	0.09 ± 0.03
South	0.13 ± 0.03	0.07 ± 0.03	0.28 ± 0.02
East	0.10 ± 0.03	0.08 ± 0.03	0.11 ± 0.02
West	0.03 ± 0.02	0.03 ± 0.02	0.03 ± 0.02
Mean value	0.08 ± 0.03		

[a]Min, minimum; max, maximum.

tal measurements made at other sites, and the values that were obtained were similar to those presented by *Kaufman et al.* [1994].

4.2. Angstrom Parameters

[34] The Angstrom parameters (α, β) were calculated using the log-log fit of the experimental AOD values against wavelength following the Angstrom law:

$$\mathrm{AOD}(\lambda) = \beta\lambda^{-\alpha} \tag{2}$$

[35] From an analysis of the spectral AOD curves it was observed that sometimes a discontinuity occurred at around 560 nm. As examples, Figure 3 shows the spectral AOD values obtained for 28 and 30 April and 23 May. This characteristic did not appear systematically, since it was only observed in half the cases, in fact during the first seven observation days. This phenomenon has been observed on other occasions, albeit in a more sporadic form, by other authors [*Pedrós et al.*, 2003; *Moorthy et al.*, 2003; *Smirnov et al.*, 2003]. The causes that could produce this discontinuity could be as follows:

[36] 1. Changes in the LI-COR 1800 filter, since one of these is at 558 nm. This should not cause a large difference between nearby values since the instrument bandwidth is 6 nm and the values are obtained every 1 nm. Furthermore, it was not observed on all the measurement days although all measurements were given for all days.

[37] 2. Physical reasons, such as, for example, the presence in the atmosphere of aerosols with different characteristics [*Pedrós et al.*, 2003; *Osterwald and Emery*, 2000]. According to *Moorthy et al.* [2003] the AOD and α values depend on the air mass origin if the spectral range is below 750 nm. Similar results have been observed in a study performed in maritime environments [*Smirnov et al.*, 2003].

[38] Fits were performed for four different spectral intervals. The spectral ranges used and the labels that they were given were as follows: (1) VIS, 340–670 nm; (2) VIS1, 340–560 nm; (3) VIS2, 560–670 nm; and (4) UV, 340–400 nm.

[39] Other authors [*Pedrós et al.*, 2003; *Vergaz*, 2001] have used different spectral intervals for calculating the Angstrom coefficients (especially referring to the wavelength exponent α). The choice of intervals is mostly motivated by the discontinuity observed in the curve of the experimental AOD values against wavelength at around 560 nm, which we believe could be related to the different modes observed in the size distribution. Specifically, if short wavelengths are considered, they provide information on the smaller particles while when longer wavelengths are used the information obtained corresponds to larger particles.

4.3. Aerosol Size Distribution

[40] The aerosol size distribution can be found from the measurements of solar radiation extinction through the formulation of the Mie theory for spectral AOD by solving the equation

$$\mathrm{AOD}(\lambda) = \int_0^r \pi r^2 Q_{ext}(r,\lambda,m) n_c(r) dr \tag{3}$$

where $Q_{ext}(r,\lambda,m)$ is the Mie extinction efficiency factor, m is the complex refraction index and $n_C(r)$ represents the number of particles per unit radius and unit area contained in the total atmospheric column. The inversion of (3) is an example of an ''ill posed problem'' where $Q_{ext}(r,\lambda,m)$ is the kernel and $n_C(r)$ is the function to be found. To solve equation (3), the inversion algorithm proposed by *King et al.* [1978] and *King* [1982] was used, employing a complex refraction index of 1.45 + 0i. In order to study the influence of the refraction index on the Mie extinction factor, the

Table 5. Average Daily Values of α

	VIS (340–670 nm)		VIS1 (340–560 nm)		VIS2 (560–670 nm)		UV (340–400 nm)	
Day	α Mean	r	α Mean	r	α Mean	r	α Mean	r
28 April 2002	1.57 ± 0.01	0.90	1.76 ± 0.01	0.96	1.27 ± 0.04	0.68	1.44 ± 0.02	0.99
30 April 2002	1.62 ± 0.06	0.97	1.65 ± 0.01	0.99	1.52 ± 0.03	0.94	1.31 ± 0.01	0.95
4 May 2002	1.85 ± 0.04	0.71	−0.55 ± 0.14	0.96	−0.55 ± 0.14	0.21	2.73 ± 0.04	0.94
8 May 2002	1.32 ± 0.03	0.77	1.69 ± 0.05	0.96	−0.28 ± 0.09	0.24	1.97 ± 0.03	0.92
15 May 2002	1.57 ± 0.02	0.90	1.91 ± 0.01	0.97	1.21 ± 0.06	0.62	1.58 ± 0.02	0.95
23 May 2002	2.01 ± 0.02	0.85	2.52 ± 0.02	0.98	0.17 ± 0.07	0.86	1.73 ± 0.02	0.93
26 May 2002	1.52 ± 0.02	0.94	1.68 ± 0.02	0.98	1.26 ± 0.06	0.81	1.57 ± 0.02	0.98
27 May 2002	1.69 ± 0.02	0.90	2.24 ± 0.03	0.97	0.85 ± 0.08	0.45	1.53 ± 0.03	0.88
28 May 2002	2.06 ± 0.06	0.76	1.79 ± 0.02	0.93	0.40 ± 0.20	0.11	2.35 ± 0.06	0.73
29 May 2002	1.53 ± 0.03	0.89	1.77 ± 0.05	0.99	1.21 ± 0.11	0.60	2.23 ± 0.04	0.92
30 May 2002	1.69 ± 0.03	0.91	1.90 ± 0.05	0.96	1.42 ± 0.12	0.57	2.34 ± 0.04	0.92
31 May 2002	1.46 ± 0.03	0.85	1.85 ± 0.05	0.95	0.66 ± 0.11	0.41	2.52 ± 0.04	0.92
1 June 2002	1.77 ± 0.03	0.92	2.06 ± 0.02	0.97	1.15 ± 0.08	0.62	1.91 ± 0.03	0.90
7 June 2002	1.74 ± 0.02	0.89	2.05 ± 0.04	0.97	0.77 ± 0.09	0.60	2.25 ± 0.03	0.96

Table 6. Average Daily Values of α, Classified as a Function of the Air Mass Origin

Air Mass Origin	VIS (340–670 nm)			VIS1 (340–560 nm)			VIS2 (560–670 nm)			UV (340–400 nm)		
	α Mean	α Min	α Max	α Mean	α Min	α Max	α Mean	α Min	α Max	α Mean	α Min	α Max
North	1.75 ± 0.03	1.46 ± 0.03	2.06 ± 0.06	1.96 ± 0.04	1.77 ± 0.05	2.52 ± 0.02	0.77 ± 0.12	0.16 ± 0.07	1.42 ± 0.12	2.23 ± 0.04	1.73 ± 0.02	2.52 ± 0.04
South	1.66 ± 0.03	1.57 ± 0.01	1.77 ± 0.03	1.89 ± 0.02	1.65 ± 0.01	2.06 ± 0.02	1.18 ± 0.06	0.77 ± 0.09	1.52 ± 0.03	1.70 ± 0.02	1.31 ± 0.01	2.25 ± 0.03
East	1.65 ± 0.02	1.52 ± 0.02	1.69 ± 0.03	1.96 ± 0.02	1.68 ± 0.02	2.24 ± 0.03	1.05 ± 0.07	0.85 ± 0.08	1.26 ± 0.06	1.55 ± 0.03	1.53 ± 0.03	1.57 ± 0.02
West	1.59 ± 0.03	1.32 ± 0.03	1.85 ± 0.04	1.14 ± 0.19	−0.55 ± 0.14	1.69 ± 0.01	0.42 ± 0.11	−0.28 ± 0.09	−0.55 ± 0.14	2.35 ± 0.04	1.97 ± 0.03	2.73 ± 0.04
Mean value	1.66 ± 0.03			1.74 ± 0.07			0.85 ± 0.09			1.96 ± 0.03		

variations of $Q_{ext}(r, \lambda, m)$ with r have been analyzed for different values of m and for a fixed wavelength. The results show that the influence is higher the lower the particle's size, reaching asymptotic values for radii bigger than 8 μm. The fastest confluence corresponds to the imaginary component of the refractive index.

[41] The influence of the refractive index of the particles on the inversion scheme has been treated by *Yamamoto and Tanaka* [1969] and by *King et al.* [1978]. They show that the shape of the retrieved aerosol size distribution was not substantially altered under various assumptions for the refractive indices. The sensitivity of the refractive index is quite weak, affecting the inverting size distribution slightly by shifting its magnitude and radii while maintaining its overall shape. The imaginary part has no impact on the retrieval size as long as particles are small. If particles are larger (>1.0 μm), the impact is still negligible when they are not highly absorbing [*Tanré et al.*, 1996]. *Gonzalez and Ogren* [1997] have analyzed, by means of simulation processes, how a wrong assumption of the refractive index affects the errors in the retrieved parameters from the King algorithm. For a bimodal size distribution the results were more sensitive to the uncertainties in the real part of the refractive index than to the uncertainties in the imaginary part.

[42] Consequently, the complex refractive index of the aerosol particles was wavelength and size independent and was given by m = 1.45 + 0.0i. This value has been used previously in other size distribution inversion works [*Cachorro and de Frutos*, 1994; *Kaufman et al.*, 1994]. Some authors have considered similar values for m with a null imaginary part [*King et al.*, 1978; *Spinhirne and King*, 1985].

[43] The inversion process was carried out by using four wavelengths (440, 670, 870 and 1020 nm), which are those normally used by the CIMEL photometers in the AERONET network [*Holben et al.*, 1998]. We divided the radii into 20 equal subintervals in the range 0.1–3 μm, an interval that was chosen after applying the *Heintzenberg et al.* [1981] criteria to the extreme wavelengths (440–1020) used in the inversion. For the smallest radii the relatively small error reflects the existence of sufficient information content that it would have been possible to perform the inversion using a small minimum radius [*Martínez-Lozano et al.*, 1999]. The alternative of employing the inversion algorithms corresponding to lower radius values is of no use since it has been demonstrated that the inversion applied to radius values outside a certain range (values that are too high or too low) generates instabilities in the solution. In such cases it is usual that the number of particles corresponding to higher radius intervals show divergences [*King*, 1982]. The increasingly large standard deviation in the size distribution at r >3 μm are to be expected from the decreasing information content of the kernel functions for these radii. However, inversions performed only up to r = 2 μm often lead to unsatisfactory and unstable solutions. The radius range of the atmospheric particulate that contributes the most significantly to the Mie optical thickness measurements is itself a function of the aerosol size distribution. For a set of optical thickness measurements over a given spectral range, the upper and lower limits for sensitivity are not necessarily fixed as

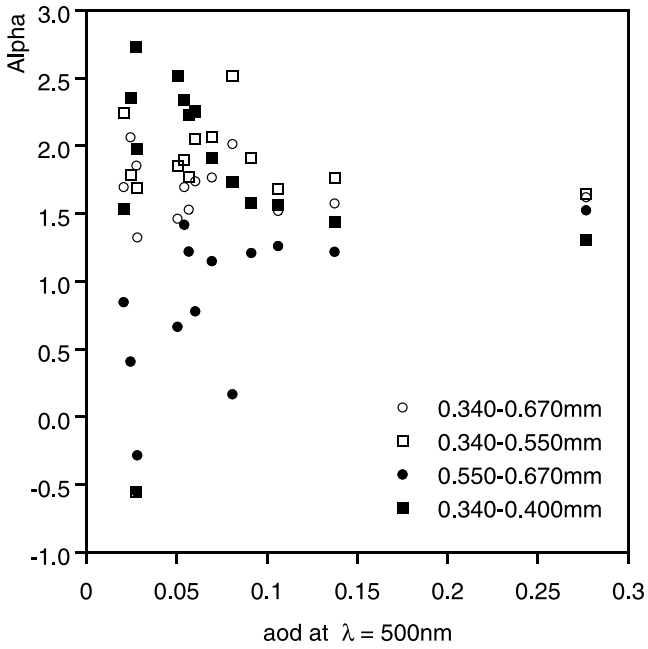

Figure 6. Evolution of the α values as a function of AOD at 500 nm.

implied by *Yamamoto and Tanaka* [1969] but instead vary depending on the form of the unknown size distribution [*King et al.*, 1978].

[44] In order to use the size distribution in volume function, assuming spherical particles, it is sufficient to perform the transformation

$$V_c(r) = \frac{4}{3}\pi r^3 n_c(r) \quad (4)$$

5. Results and Discussion

5.1. Spectral Aerosol Optical Depth

[45] The analysis of the AOD was based on its spectral behavior and the change in value for different wavelengths, specifically 340, 440, 500, 670 and 1020 nm. Figure 4 shows the evolution of the average daily AOD values for these wavelengths. As can be seen, in general, the AOD values obtained at 500 nm were quite low throughout the campaign, oscillating between 0.02 and 0.28 (see Table 3). The highest values were observed on the first days of the campaign, 28 April 2002 and 30 April 2002 (Figure 3). This could have been due to the residual background aerosol load that had accumulated in the area because of the stability of the Arctic atmosphere in winter. Excluding these two days, the maximum AOD value was 0.11.

[46] Figure 5 shows the spectral AOD values grouped as a function of the origins of the air masses. The highest AOD values were had when the air masses came from the south. These aerosols are of continental type and come from central Europe and Russia. The lowest AOD values corresponded to the air masses coming from the west. According to the back trajectories, in this case, a mixture of continental- and maritime-type aerosols could be expected since the air masses had crossed the Atlantic Ocean and the Scandinavian Peninsula. Table 4 shows the average, maximum and minimum values of AOD at 500 nm according to air mass origin.

5.2. Angstrom Wavelength Exponent

[47] As indicated previously, fits were made at four different spectral intervals, with the aim to observe whether the different types of aerosol influence certain spectral ranges. Tables 5 and 6 present summaries of the average daily values for the several intervals.

[48] 1. The α values observed in the VIS spectral region (340–670 nm) were found to stay in a relatively narrow range between 1.32 and 2.06, values that correspond to small-size aerosols.

[49] 2. By using only the VIS1 spectral region (340–560 nm), a notable improvement in the correlation coefficients of the fit was obtained, up to between 0.93 and 0.99. In general, the values obtained for α in this region were higher than those calculated for the whole spectrum. All values were higher than 1.6 except that observed on 4 May 2002 with a value of −0.55. This negative value indicates a predominance of large particles over the accumulation mode. For all other days of the campaign the accumulation mode was dominant.

Table 7. Modal Parameters for Each Day of the Campaign: Accumulation and Coarse Modes

	Accumulation Mode				Coarse Mode			
Day	V_0, cm^3 cm^{-2}	σ	r_m, μm	r	V_0, cm^3 cm^{-2}	σ	r_m, μm	r
28 April 2002	(6.1 ± 5.0) e-5[a]	3.6 ± 0.9	0.018 ± 0.015	0.99	(1.22 ± 0.02) e-5	17.0 ± 0.6	2.46 ± 0.04	0.99
30 April 2002	(5.1 ± 3.0) e-5	2.8 ± 0.9	0.040 ± 0.030	0.99	(5.9 ± 4.0) e-6	5.50 ± 0.50	0.50 ± 0.07	0.99
4 May 2002	(9.6 ± 0.2) e-7	2.0 ± 0.1	0.104 ± 0.002	0.99	(1.5 ± 0.7) e-5	2.57 ± 0.06	3.97 ± 0.19	0.99
8 May 2002	(9.6 ± 1.4) e-6	1.7 ± 0.1	0.075 ± 0.006	0.99	(2.6 ± 0.3) e-5	2.16 ± 0.11	3.12 ± 0.30	0.99
15 May 2002	(1.8 ± 1.1) e-5	2.7 ± 0.1	0.045 ± 0.004	0.99	(1.6 ± 0.5) e-5	3.03 ± 0.17	4.90 ± 0.70	0.99
23 May 2002	(8.9 ± 1.1) e-6	1.7 ± 0.1	0.072 ± 0.005	0.99	(1.10 ± 0.04) e-5	1.93 ± 0.05	2.36 ± 0.07	0.99
26 May 2002	(1.5 ± 0.9) e-5	2.7 ± 0.7	0.050 ± 0.030	0.99	(7.8 ± 0.1) e-6	6.50 ± 010	5.37 ± 0.14	0.99
27 May 2002	(1.5 ± 0.8) e-5	3.6 ± 0.9	0.030 ± 0.020	0.99	(1.9 ± 0.1) e-5	5.30 ± 0.30	9.90 ± 1.20	0.99
28 May 2002	(2.6 ± 0.5) e-6	2.4 ± 0.1	0.075 + 0.001	0.99	(2.80 ± 0.09) e-6	2.50 ± 0.07	2.80 ± 0.07	0.99
29 May 2002	(3.2 ± 0.1) e-6	2.1 ± 0.1	0.148 ± 0.005	0.99				
30 May 2002	(2.9 ± 0.2) e-6	1.8 ± 0.1	0.154 ± 0.001	0.98				
31 May 2002	(2.7 ± 0.1) e-6	2.0 ± 0.1	0.200 ± 0.006	0.99				
1 June 2002	(9.1 ± 4.0) e-6	1.9 ± 0.2	0.060 ± 0.020	0.99	(1.2 ± 0.6) e-5	2.32 ± 0.07	2.78 ± 0.13	0.99
7 June 2002	(1.9 ± 1.2) e-5	2.5 ± 0.4	0.035 ± 0.020	0.99	(8.2 ± 0.3) e-6	3.98 ± 0.13	4.67 ± 0.27	0.99

[a]Read (6.1 ± 5.0) e-5 as (6.1 ± 5.0) × 10^{-5}.

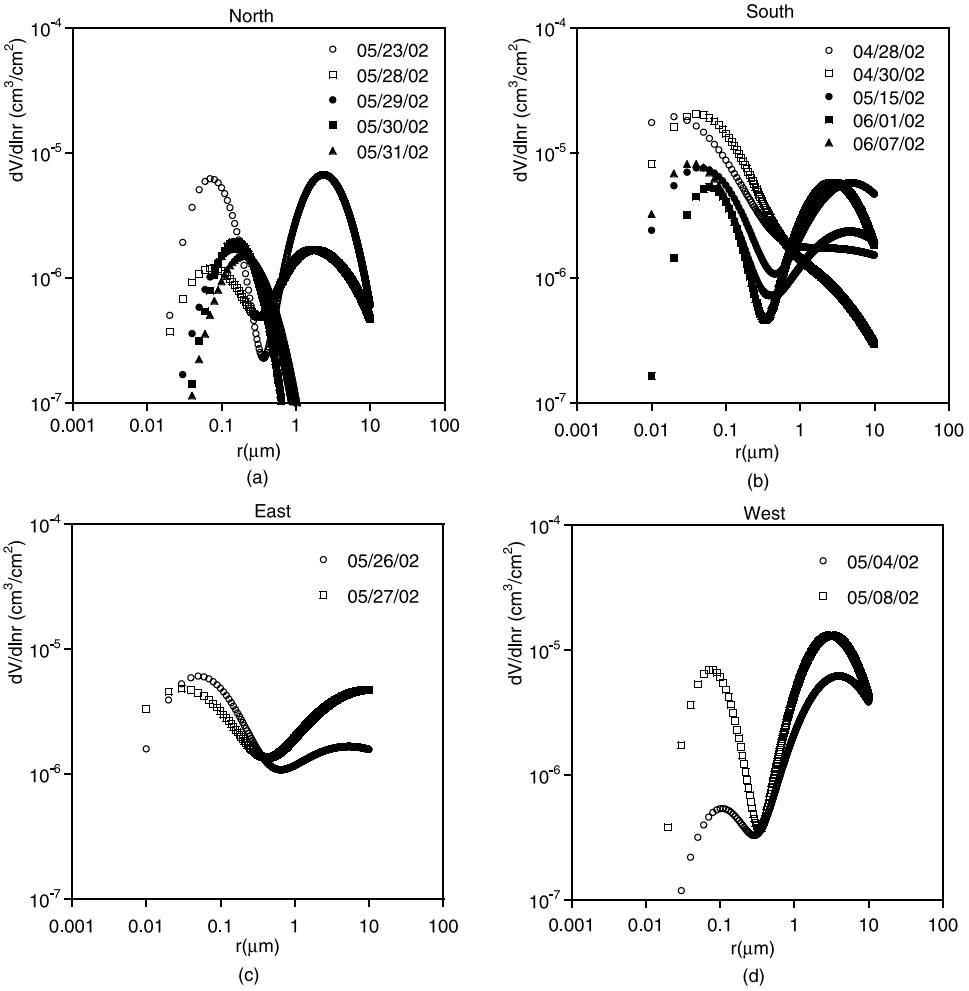

Figure 7. (a–d) Size distribution (in volume) grouped according to air mass origin.

[50] 3. In general, the behavior of the AOD in the VIS2 spectral region (560–670 nm) was much flatter than in the 340–560 nm interval, for which reason α took lower values. All were less than 1.5, even reaching negative values when there is a change of curvature of the AOD(λ) function.

[51] 4. In general, high values of α, above 1.3, were observed in the UV spectral region (340–400 nm). This indicated the presence of fine particles. Furthermore, for the fits in this interval the correlation coefficients were between 0.90 and 0.95.

[52] The dispersion of the α values for the VIS and VIS1 intervals was less pronounced than that presented by the α values in the VIS2 and UV intervals, indicating that the latter had a greater dependence with respect to the AOD than the former which seem to be independent of it. Whatever the case, the α values of all the intervals used are independent of the interval chosen for high AOD values as is shown in Figure 6.

5.3. Aerosol Size Distribution

[53] First, the size distributions by volume were calculated for each of the measurements made and subsequently daily average values were obtained using all these size distributions. Once these daily average values had been obtained, fits were made of the size distribution function as a function of radius assuming that this follows a lognormal behavior, given by the expression (for each mode)

$$\frac{dV}{dlogr} = \frac{V_0}{\sqrt{2\pi}\log\sigma} \exp\left[-\frac{1}{2}\left(\frac{\log r - \log r_m}{\log\sigma}\right)^2\right] \quad (5)$$

[54] From the fit mentioned, we obtained the modal parameters V_0, r_m and σ, which represent the maximum particle concentration, the radius of the mode and the standard deviation, respectively. Table 7 shows the values of these fits for the accumulation and coarse modes. At the same time, Figure 7 represents these fits in relation to the air mass origin.

5.3.1. Radius of the Mode

[55] In general, the size distributions by volume found by the above described inversion process showed a bimodal behavior for almost all of the days studied. Only on the three days 29 May 2002, 30 May 2002 and 31 May 2002 were monomodal distributions observed. As an example, Figure 8 illustrates the size distribution corresponding to 30 May 2002. Curiously, these days correspond to cases

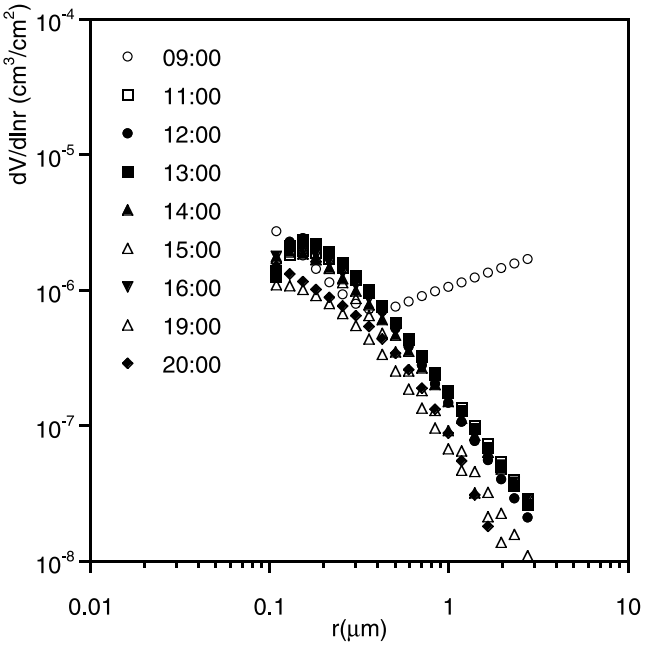

Figure 8. Size distribution for 30 May 2002.

where the air mass came from the north. It has been estimated that for the whole set of campaign days the average radius value of the accumulation mode was in the interval [0.02, 0.2] μm while the coarse particle mode the average radius value fell in the wider range of [2.4, 20] μm.

[56] Bearing in mind the information obtained from the back trajectories, the modal parameters of each mode of the volume distribution have been classified according to the origins of the air masses, in the same way that the aerosol parameters (AOD and α) were analyzed.

[57] With respect to the accumulation mode it is worth highlighting various characteristics. First, the values were above 0.99 for the correlation coefficient of the lognormal function fits. Second, similar behavior in the modal radius was observed depending on the direction they came from (by south-east and north-west pairs).

[58] If the aerosols came from the south or east, the radius of the mode took small values, with averages between 0.04 ± 0.02 μm and 0.04 ± 0.03 μm respectively, as can be seen in Table 8. This is a logical consequence given that the aerosols present must be of the same continental or industrial type. The errors obtained for these values were of the order of the values themselves since the lower radius limit used in the inversion was 0.1 μm. In these circumstances the curves were not well defined and the lognormal fits had to be made with less than the optimum number of points with a consequent increase in error.

[59] For the air masses coming from the north and west directions, Arctic and maritime-type aerosols were expected. For this reason, in both cases a similar behavior of the radius was observed. However, in these cases the average modal radius was quite a lot bigger than for the air masses coming from the south or east, 0.13 ± 0.01 μm (north) and 0.09 ± 0.01 μm (west).

[60] The fit for the coarse particles is more complex than for the accumulation mode, since it is often made with less experimental points than desirable due, mainly, to the upper limit of the radius interval used in the inversion. If it is remembered that throughout the campaign the average modal radius for the coarse particle mode was 4.17 μm and that in addition 3 μm was taken as the upper radius for the inversion, then the coarse particle mode could be represented by barely 5 or 6 points and so could only be shown lightly. This is why the error obtained when the modal radius was much higher than 3 μm increased considerably, as shown in Table 8.

[61] In this case no similarity was seen between the different directions of the air masses. The intervals for the modal radius were wider and had average values in the range [2.36 and 9.9] μm, excepting the value corresponding to 30 April 2002, which was an exceptionally low 0.5 μm. Another exceptional circumstance was the already noted nonappearance of a coarse particle mode on the days 29 May 2002, 30 May 2002 and 31 May 2002.

5.3.2. Size Distribution Volume

[62] Another of the lognormal fit parameters is the volume (V_0) of each of the distribution modes. Unlike the modal radius the volume of the distribution does not have such a strict dependence on the particle type present in the atmosphere, depending more on the quantity of particles than on their type. For this reason, it is more useful to qualitatively relate the importance of each of the modes in the total distribution than to analyze in detail the quantitative values of the volume of each mode. In general, a bimodal behavior was observed for the size distribution function. However, a series of characteristics was found, as a function of the origins of the air masses, that is worth detailing.

[63] 1. For some of the days when the air masses proceeded from the north, the coarse particle mode was

Table 8. Accumulation and Coarse Mode Modal Radius as a Function of Air Mass Origin

	Accumulation Mode			Coarse Mode		
Air Mass Origin	r_m, μm	r_m Min, μm	r_m Max, μm	r_m, μm	r_m Min, μm	r_m Max, μm
North	0.13 ± 0.01	0.07 ± 0.01	0.20 ± 0.01	2.58 ± 0.07	2.36 ± 0.07	2.80 ± 0.07
South	0.04 ± 0.02	0.02 ± 0.02	0.06 ± 0.02	2.9 ± 0.3[a]	2.46 ± 0.04[a]	4.9 ± 0.7[a]
East	0.04 ± 0.03	0.03 ± 0.3	0.05 ± 0.03	7.6 ± 0.7	5.4 ± 0.1	9.9 ± 1.2
West	0.09 ± 0.01	0.08 ± 0.01	0.10 ± 0.01	3.5 ± 0.2	3.1 ± 0.3	3.9 ± 0.2
Mean value	0.08 ± 0.01			4.2 ± 0.3		

[a]To calculate the average value corresponding to the south direction, the value of the modal radius corresponding to 30 April 2002 was not used as this corresponded to the coarse-particle-type mode.

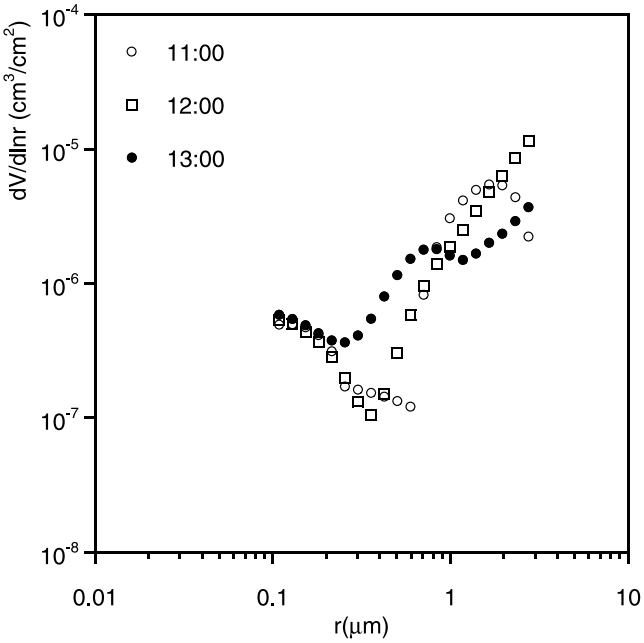

Figure 9. Size distribution for 4 May 2002, with air masses coming from the west.

seen to disappear. This could be explained by the fact that the air masses coming from the Arctic Ocean are very dry and carry hardly any small particles, so the observed mode would be dominated by local particle types.

[64] 2. Generally, in the air masses from the south, the accumulation mode is determinant being of much more importance than the coarse particle mode. In fact, some accumulation modes hide under their wings very small modes that, in some cases and because of the small size of the radius, can only be assigned to conventional coarse particle modes with difficulty. This circumstance is more important the greater the optical depth observed, so it would appear clear that in this case the accumulation mode is the principal cause of the radiation extinction by aerosols.

[65] 3. In the air masses from the east, the volume distribution showed that the accumulation mode had a greater importance than the coarse mode. However, in this case the coarse mode was always seen clearly.

[66] 4. In the air masses from the west, unlike the other cases, it was seen that the coarse particle mode contributed to a greater extent to the total aerosol volume. It is usual to observe a doubling up of this mode (Figure 9). As the day goes on, the coarse particle mode grows and moves toward larger radii. These changes to the second mode can be translated into a substantial variation in the AOD, especially at short wavelengths.

5.3.3. Standard Deviation

[67] The standard deviation of a lognormal function represents the width of the mode. In general, it was seen that the standard deviation corresponding to the coarse particle mode was slightly higher than that corresponding to the accumulation mode. Generally, the coarse particle mode had a higher standard deviation with an average of 4.2 while the accumulation mode average was 2.6. In Table 9 the standard deviations are presented classified according to the air mass origin, for the accumulation and coarse modes. Also in this case a similarity was observed between the directions north-west and south-east. For the directions north and west, both the accumulation and the coarse mode were narrower than for the directions south and east.

5.3.4. Effective Radius of the Distribution

[68] The effective radius relates the quotient between the total volume of the particles and their surface:

$$r_{eff}=\frac{\int_0^\infty \pi r^3 \frac{dN}{dr}\,dr}{\int_0^\infty \pi r^2 \frac{dN}{dr}\,dr}=\frac{3}{4}\frac{V}{S} \tag{6}$$

Thus it gives us an idea of the average size of the particles that contribute in the extinction process. Using the relations

$$\frac{dN}{dlogr}=rln10\frac{dN}{dr} \tag{7}$$

$$\frac{dV}{dlogr}=\frac{4}{3}\pi r^3\frac{dN}{dlogr} \tag{8}$$

[69] The effective radius can be expressed in the form

$$r_{eff}=\frac{\int_0^\infty \pi \frac{1}{r}\frac{dV}{dlogr}\,dr}{\int_0^\infty \pi \frac{1}{r^2}\frac{dV}{dlogr}\,dr} \tag{9}$$

[70] The effective radius was obtained for the total distribution and for each of the modes separately. In the latter case we used the theoretical expression for the effective radius obtained by calculating the quotient of the integrals using the lognormal distribution function

$$r_{eff}=r_m\exp\left[2.5\ln^2(\log\sigma)\right] \tag{10}$$

Table 9. Standard Deviation for the Accumulation and Coarse Modes as a Function of Air Mass Origin

	Accumulation Mode			Coarse Mode		
Air Mass Origin	σ	σ Min	σ Max	σ	σ Min	σ Max
North	2.02 ± 0.06	1.77 ± 0.05	2.37 ± 0.02	2.25 ± 0.06	1.93 ± 0.05	2.50 ± 0.07
South	2.7 ± 0.5	1.97 ± 0.2	3.6 ± 0.9	6.4 ± 1.2	2.32 ± 0.07	17.0 ± 0.6
East	3.1 ± 0.6	2.7 ± 0.7	3.6 ± 1.0	5.90 ± 0.08	5.3 ± 0.3	6.5 ± 0.1
West	2.40 ± 0.04	2.05 ± 0.03	1.73 ± 0.06	2.37 ± 0.09	2.16 ± 0.11	2.57 ± 0.06
Mean value	2.6 ± 0.3			4.2 ± 0.4		

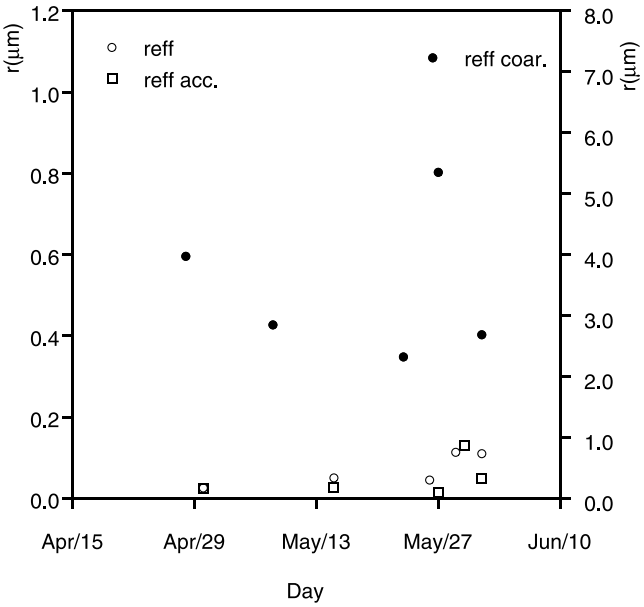

Figure 10. Evolution over the whole campaign of effective total radius for each mode.

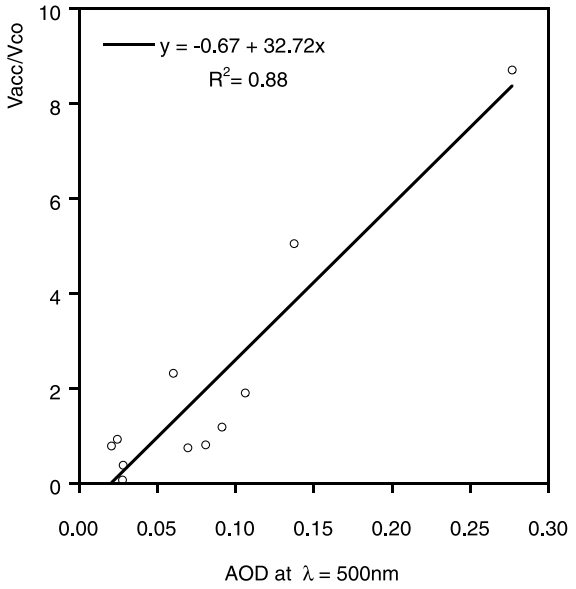

Figure 12. Volume quotient (V_{acc}/V_{co}) as a function of AOD at 500 nm.

where r_m is the radius of the mode when the size distribution is given in number of particles. This can be related to the modal radius of the volume distribution assuming that the particles are spherical:

$$r_v = r_m \exp\left(-3\log^2\sigma\right) \tag{11}$$

[71] In general, the effective radius took quite low values, always less than 0.2 μm. Only twice did it take higher values, with 0.88 μm and 1.05 μm (see Figure 10). These higher values were only observed when the coarse particle mode predominated over the total distribution volume. This result confirms that, in general, the aerosols that predominated in the study area were the small ones, independent of the origin of the air masses.

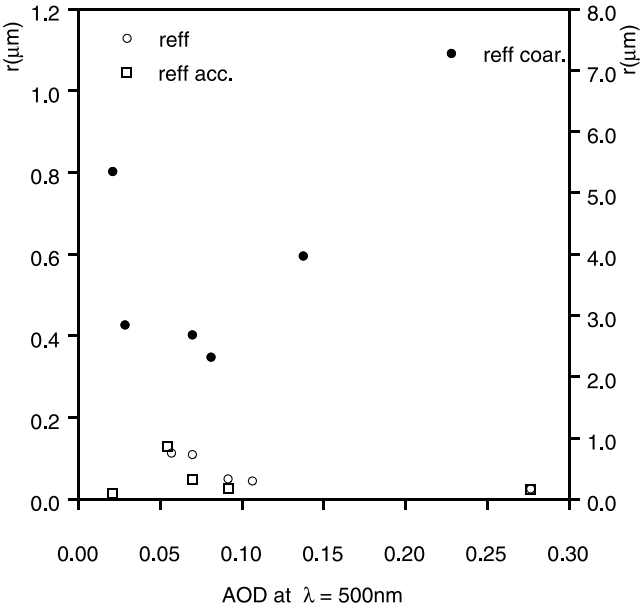

Figure 11. Evolution of effective total radius and the effective radius for each mode against AOD at 500 nm.

[72] The effective radii corresponding to the accumulation mode were lower than 0.07 μm except those obtained for the three days in which only one mode was observed in the size distribution, when it took values between 0.1 μm and 0.15 μm. This is a logical consequence given that in these cases the observed mode had been displaced toward higher radii. With respect to the effective radius corresponding to the coarse particle mode this was observed to be quite variable, with values between 1.8 μm and 5.3 μm.

[73] When the variation of the total effective radius and the effective radii for the different modes were analyzed with respect to the AOD at different wavelength (440, 500 and 670 nm), the former were observed to diminish as the aerosol load increased. This decrease was much more pronounced for the total r_{eff} and for the accumulation mode, while it was quite smooth for the coarse particle mode (see Figure 11). In this way the greater the observed AOD the greater importance had the small particles in relation to the solar radiation extinction. No difference in the trend was observed by varying the wavelength used.

[74] Another way of determining which of the particle types plays the most important role is to observe the behavior of the quotient between the volumes of each of the modes (V_{acc}/V_{co}) against the AOD. This quotient is directly proportional to the AOD, such that the greater the AOD, the greater will be the importance of the small particles and therefore it will be this mode that controls

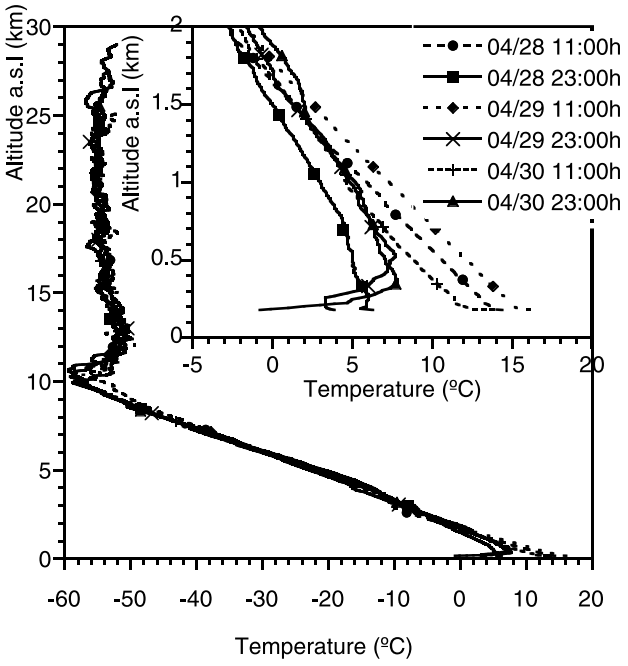

Figure 13. Vertical profile of temperature from sounding data on 28, 29, and 30 April 2002.

the greater part of the aerosol extinction mechanisms (see Figure 12).

5.4. Possible Arctic Haze Short Episode

[75] In order to determine the cause of the observed aod increase, we aimed our analysis in two ways. First, we analyzed in detail the (air mass) backward trajectories reaching the area before and after the episode. Second, we examined the vertical structure of the lowermost atmosphere.

[76] The air mass analysis from 25 April to 1 May reveals an important change in the meteorological situation at noon on 28 April, favoring the arrival of air masses from eastern Europe and Russia. This situation remains steady until the end of 30 April. It actually persists longer, but these days were not of interest for our study because the skies were cloudy and we could not take measurements.

[77] We have studied the temperature and relative humidity (RH) profiles in the lowermost atmosphere from the sounding data. There are some interesting features that would have caused the increase in the aerosol loading. The high values of RH ($\sim$100%) and the temperatures (from -1°C to 8°C) observed in the lower atmospheric layer show a favorable situation for the condensation of water vapor and haze formation by the night of 28 April (Figure 13). The haze caused the evolution of cumulus during an important part of the day, covering a great part of the sky dome. However, the nocturnal temperature profiles of 29 and 30 April show a surface inversion layer of 300 m and 200 m depth respectively (Figure 13). This feature points out that the lowermost layer and the upper one are totally uncoupled, because of the role of transport from south, which we previously commented on. Furthermore, the thermal profiles at noon do not change substantially at heights upper than 500 or 600 m, respect to the profiles observed at night. Therefore the convective mixture during the day is very limited and the role of synoptic transport is not altered by the disappearance of those inversion layers during the day.

[78] A strong contribution of the accumulation mode is observed in the aerosol size distribution for those days. A soft rainfall during the night of 29 April 2002 seems to be the responsible of the volume decreasing of the coarse mode between 28 April 2002 and 30 April 2002 (Figure 7) causing a great lose of coarse particles that can explain the AOD decrease measured between those days (Figure 5).

[79] The AOD increase observed during 28 and 30 April is mainly due to the synoptic transport of pollution aerosols from the industrial areas of Ukraine and the occidental part of Russia. However, this concentration of very small particles is also supported by the residual layer where the accumulation of aerosols from local sources was favored, contributing to the total aerosol loading.

6. Conclusions

[80] A study has been made of the column aerosols using measurements of solar irradiance extinction at ground level in the boreal region (Sodankylä, Finland), during the spring of 2002, relating the properties of the same to the origins of the air masses. In general, we observed very low levels of aerosols, independent of the air mass origin, with AOD values at 500 nm below 0.09. Higher values were only observed during the first days of the campaign, at the end of April, a fact that could be explained by the residual accumulation of particles coming from Russia and central Europe during the winter with a stable atmosphere.

[81] A sharp change in the slope of the spectral AOD curve was observed at 560 nm, which could be due to the presence of various types of aerosols with differing spectral behaviors with respect to solar radiation. This discontinuity was independent of the air mass origins although it appeared to show a certain time dependence, since it was only detected during the first half of the campaign.

[82] We also observed a similar behavior in the aerosols when they came in air masses from the north-west or the south-east. In the first case (proceeding from the north and west) the aerosol load was very small with very low optical depths of around 0.03–0.09 for 500 nm wavelengths. The size distribution usually showed two modes with a strong contribution from the coarse particle mode probably as a consequence of the presence of maritime-type particles coming from the ocean. This circumstance was especially relevant for air masses coming from the west. In the case of air masses coming from the north, the second mode disappeared in some cases, a circumstance that could be related to the low evaporation that occurs in the Arctic Ocean, as well as the low relative humidity that restricts the hygroscopic growth of the minimal load of salt particles present in the air.

[83] When the air masses came for southerly or easterly directions, they had a completely opposite behavior to those observed in the previous case. In these cases the AOD was rather larger, above all for air masses coming from central Europe and Russia with a value at 500 nm of 0.134. When the air masses came from the east, the average value was

0.095. These results seem to indicate that in both cases the air masses were charged with anthropogenic aerosols such that the accumulation mode acquired greater importance. In fact it could be observed that the coarse particle mode decreased in volume throughout the day as well as reducing the modal radius. This decrease was associated with a daily decrease of the AOD, above all at short wavelengths.

[84] Important daily variations were observed in the size distribution, especially in the second mode, and this fact was reflected in spectral AOD fundamentally for wavelengths less than 670 nm, while for longer wavelengths there were hardly any fluctuations. This characteristic was independent of the type of air mass considered, thus it seemed to be due to atmospheric instability causing the deposition of coarse particles coming from local sources and with short average lifetimes in the atmosphere.

[85] **Acknowledgments.** The Sodankylä SIFLEX campaign was organized and supported by ESA. The authors gratefully acknowledge the personnel of the Finnish Meteorological Institute at Sodankylä Geophysical Observatory for their scientific data and the use of their facilities, especially its director Esko Kyrö. We also gratefully acknowledge the NOAA Air Resources Laboratory (ARL) for provision of the HYSPLIT transport and dispersion model and/or READY Web site (http://www.arl.noaa.gov/ready.html) used in this publication. Special thanks go to Manuel Pujadas from Centro de Investigaciones Energéticas, Medioambientales y Tecnologicas (CIEMAT) for his invaluable contributions to the vertical profile analysis studied in this work.

References

Anderson, S. M., and K. Mauersberger (1992), Measurements of ozone absorption cross section in the Chappuis band, *Geophys. Res. Lett.*, *19*, 933–936.

Aurela, M., T. Laurila, and J. Tuovinen (2002), Annual CO_2 balance of a subarctic fen in northern Europe: Importance of the wintertime efflux, *J. Geophys. Res.*, *107*(D21), 4607, doi:10.1029/2002JD002055.

Bodhaine, B. A., N. B. Wood, E. G. Dutton, and J. R. Slusser (1999), On Rayleigh optical depth calculations, *J. Atmos. Oceanic Technol.*, *16*, 1854–1861.

Cachorro, V. E., and A. M. de Frutos (1994), Retrieval of the atmospheric aerosol characteristics from visible extinction data at Valladolid (Spain), *Atmos. Environ.*, *28*, 963–971.

Davidson, M., et al. (2002), The Solar Induced Fluorescence Experiment (SIFLEX-2002), *Eur. Space Agency Spec. Publ., ESA SP-527*, 1–12.

European Space Agency (2002), Flex Workshop, *Eur. Space Agency Spec. Publ., ESA SP-527*.

Gonzalez, H., and J. A. Ogren (1997), Sensitivity of retrieved aerosol properties to assumptions in the inversion of spectral optical depths, *J. Atmos. Sci.*, *53*, 3669–3685.

Gueymard, C. A. (2001), Parameterized transmittance model for direct beam and circumsolar spectral irradiance, *Sol. Energy*, *71*, 325–346.

Heintzenberg, J. (1980), Particle size distribution and optical properties of Arctic haze, *Tellus*, *32*, 251–260.

Heintzenberg, J., H. Muller, H. Quenzel, and E. Thomalla (1981), Information content of optical data with respect to aerosol properties: Numerical studies with a randomized minimum-search-technique inversion algorithm, *Appl. Opt.*, *20*, 1308–1315.

Herber, A., L. W. Thomason, H. Gernandt, U. Leiterer, D. Nagel, K. H. Schulz, J. Kaptur, T. Albrecht, and J. Notholt (2002), Continuous day and night aerosol optical depth observations in the Arctic between 1991 and 1999, *J. Geophys. Res.*, *107*(D10), 4097, doi:10.1029/2001JD000536.

Holben, B. N., A. Setzer, T. F. Eck, A. Pereira, and I. Slutsker (1996), Effect of dry season biomass burning on Amazon basin aerosol concentrations and optical properties, 1992–1994, *J. Geophys. Res.*, *101*, 19,465–19,481.

Holben, B. N., et al. (1998), AERONET: A federated instrument network and data archive for aerosol characterization, *Remote Sens. Environ.*, *66*, 1–16.

Holben, B. N., et al. (2001), An emerging ground-based aerosol climatology: Aerosol optical depth from AERONET, *J. Geophys. Res.*, *106*, 12,067–12,097.

Kasten, F., and M. T. Young (1989), Revised optical air mass tables and approximation formula, *Appl. Opt.*, *28*, 4735–4738.

Kaufman, Y. J., A. Gitelson, A. Karnieli, E. Ganor, R. S. Fraser, T. Nakajima, S. Mattoo, and B. N. Holben (1994), Size distribution and scattering phase function of aerosol particles retrieved from sky brightness measurements, *J. Geophys. Res.*, *99*, 10,341–10,356.

Khattatov, V. U., A. E. Tyabatov, A. P. Alekseyew, A. A. Postnov, and E. A. Stulow (1997), Aircraft lidar studies of the Arctic haze and their meteorological interpretation, *Atmos. Res.*, *44*, 99–111.

King, M. D. (1982), Sensitivity of constrained linear inversions to the selection of Lagrange multiplier, *J. Atmos. Sci.*, *39*, 1356–1369.

King, M. D., D. M. Byrne, B. M. Herman, and J. A. Reagan (1978), Aerosol size distributions obtained by inversions of spectral optical depth measurements, *J. Atmos. Sci.*, *35*, 2153–2167.

Laurila, T., H. Soegaard, C. R. Lloyd, M. Aurela, J. P. Tuovinen, and C. Nordstroem (2001), Seasonal variations of net CO_2 exchange in European Arctic ecosystems, *Theor. Appl. Climatol.*, *70*, 183–201.

Martínez-Lozano, J. A., M. P. Utrillas, and F. Tena (1999), Retrieval of the aerosol size distribution from spectroradiometer measurements at a coastal site in the Mediterranean Sea, *Int. J. Remote Sens.*, *20*, 2167–2182.

Martínez-Lozano, J. A., et al. (2003), Intercomparison of spectroradiometers for global and direct solar irradiance in the visible range, *J. Atmos. Oceanic Technol.*, *20*, 997–1010.

Moorthy, K. K., S. S. Babu, and S. K. Satheesh (2003), Aerosol spectral optical depths over the Bay of Bengal: Role of transport, *Geophys. Res. Lett.*, *30*(5), 1249, doi:10.1029/2002GL016520.

Morys, M., F. M. Mims III, S. Hagerup, S. E. Anderson, A. Baker, J. Kia, and T. Walkup (2001), Design, calibration, and performance of MICROTOPS II handheld ozone monitor and Sun photometer, *J. Geophys. Res.*, *106*, 14,573–14,582.

Osterwald, C. R., and K. A. Emery (2000), Spectroradiometric Sun photometry, *J. Atmos. Oceanic Technol.*, *17*, 1171–1188.

Pedrós, R., J. A. Martínez-Lozano, M. P. Utrillas, J. L. Gómez-Amo, and F. Tena (2003), Column-integrated aerosol optical properties from ground-based spectroradiometer measurements at Barrax (Spain) during the Digital Airborne Imaging Spectrometer Experiment (DAISEX) campaigns, *J. Geophys. Res.*, *108*(D18), 4571, doi:10.1029/2002JD003331.

Penner, J. E., L. Reaitch, D. Murphy, J. Nganga, and G. Pitari (2001), Aerosols: Their direct and indirect effects, in *Climate Change: The Scientific Basis*, edited by J. Hougthton et al., pp. 289–348, Cambridge Univ. Press, New York.

Remer, L. A., and Y. J. Kaufman (1998), Dynamic aerosol model: Urban/industrial aerosol, *J. Geophys. Res.*, *103*, 13,859–13,871.

Remer, L. A., S. Gassó, D. A. Hegg, Y. J. Kaufman, and B. N. Holben (1997), Urban/industrial aerosol: Ground-based Sun/sky radiometer and in situ measurements, *J. Geophys. Res.*, *102*, 16,849–16,859.

Remer, L. A., Y. J. Kaufman, and B. N. Holben (1999), Interannual variation of ambient aerosol characteristics on the coast of the United States, *J. Geophys. Res.*, *104*, 2223–2231.

Ricard, V., J. L. Jaffrezo, V. M. Kerminen, R. E. Hillamo, K. Teinillä, and W. Maenhaut (2002a), Size distributions and modal parameters of aerosol constituents in northern Finland during the European Arctic Aerosol Study, *J. Geophys. Res.*, *107*(D14), 4208, doi:10.1029/2001JD001130.

Ricard, V., J.-L. Jaffrezo, V.-M. Kerminen, R. E. Hillamo, M. Sillanpaa, S. Ruellan, C. Liousse, and H. Cachier (2002b), Two years of continuous aerosol measurements in northern Finland, *J. Geophys. Res.*, *107*(D11), 4129, doi:10.1029/2001JD000952.

Ruellan, S. (2000), Etude comparative des aerosols carbonés en milieu tropical urban et artique: Spécificité des sources et evolution dans l'atmosphère, These de 3ème cycle, 195 pp., Univ. Paris VI, Paris.

Rummukainen, M., R. Kivi, and T. Laurila (1996), Yearly cycle of lower tropospheric ozone at the Arctic Circle, *Atmos. Emviron.*, *30*, 1875–1885.

Russell, P., et al. (1993), Pinatubo and pre-Pinatubo optical depth spectra: Mauna Loa measurements, comparisons, inferred particle size distributions, radiative effects, and relationships to lidar data, *J. Geophys. Res.*, *98*, 22,969–22,985.

Schmid, B., J. Michalsky, R. Halthore, M. Beauharnois, L. Harrison, J. Livingston, P. Russell, B. Holben, T. Eck, and A. Smirnov (1999), Comparison of aerosol optical depth from four solar radiometers during the fall 1997 ARM Intensive Observation Period, *Geophys. Res. Lett.*, *26*, 2725–2728.

Schwartz, S. E., and M. O. Andreae (1996), Uncertainty in climate change caused by aerosols, *Science*, *272*, 1121–1122.

Shaw, G. E. (1982), Atmospheric turbidity in the polar regions, *J. Appl. Meteorol.*, *21*, 1080–1088.

Smirnov, A., B. N. Holben, O. Dubovik, R. Frouin, T. F. Eck, and I. Slutsker (2003), Maritime component in aerosol optical models derived from Aerosol Robotic Network data, *J. Geophys. Res.*, *108*(D1), 4033, doi:10.1029/2002JD002701.

Spinhirne, J. D., and M. D. King (1985), Latitudinal variation of spectral optical thickness and columnar size distribution of the El Chinchón stratospheric aerosol layer, *J. Geophys. Res.*, *90*, 10,607–10,619.

Stoll, M.-P., A. Court, K. Smorenburg, H. Visser, L. Crocco, J. Heilimo, and A. Honig (1999a), FLEX-Fluorescence Explorer, *Proc. SPIE Int. Soc. Opt. Eng.*, *3868*, 487–497.

Stoll, M.-P., T. Laurila, B. Cunin, A. Gitelson, H. K. Lichtenthaler, and T. Hame (1999b), FLEX-Fluorescence Explorer: A space mission for screening vegetated areas in the Fraunhofer lines, *Proc. SPIE Int. Soc. Opt. Eng.*, *3868*, 108–119.

Strahler, A. H., and A. N. Strahler (1992), *Modern Physical Geography*, 4th ed., John Wiley, Hoboken, N. J.

Tanré, D., M. Herman, and Y. J. Kaufman (1996), Information on aerosol size distribution contained in solar reflected spectral radiances, *J. Geophys. Res.*, *101*, 19,043–19,060.

Tuovinen, J. P., T. Laurila, H. Lattila, A. Ryaboshapko, P. Brukhanov, and S. Korolev (1993), Impact of the sulphur dioxide sources in the Kola Peninsula on air quality in northernmost Europe, *Atmos. Environ., Part A*, *32*, 1605–1613.

Utrillas, M. P. (1995), Estudio de aerosoles a partir de medidas de irradiancia solar spectral, Ph.D. thesis, Univ. de Valencia, Burjassot, Spain.

Valkama, I., and J. Rossi (1992), Description of the model TRADOS, in *Evaluation of Long-Range Atmospheric Transport Models Using Environmental Radioactivity Data From the Chernobyl Accident: The ATMES Report*, edited by W. Klug et al., pp. 171–182, Elsevier, New York.

Vergaz, R. (2001), Optical properties of atmospheric aerosols: Characterization of Cádiz Gulf area (in Spanish), Ph.D. thesis, Univ. de Valladolid, Valladolid, Spain.

Yamamoto, G., and M. Tanaka (1969), Determination of aerosol size distributions from spectral attenuation measurements, *Appl. Opt.*, *8*, 447–453.

V. Estellés, J. L. Gómez-Amo, J. A. Martínez-Lozano, R. Pedrós, and M. P. Utrillas, Solar Radiation Group, University of Valencia, C/ Dr. Moliner 50, E-46100 Burjassot, Spain. (jmartine@uv.es)